

Article

Towards Environment Friendly Hydrothermally Synthesized Li^+ , Rb^+ , In^{3+} Intercalated Phosphotungstate ($\text{PW}_{12}\text{O}_{40}$) Thin Films

Sameer N. Nadaf¹, Satish S. Patil¹ , Vilasrao A. Kalantre², Sawanta S. Mali³ , Jyoti V. Patil^{3,4}, Chang Kook Hong³, Sharadchandra S. Patil⁵ , Popatrao N. Bhosale¹ and Sambhaji R. Mane^{1,*}

¹ Materials Research Laboratory, Department of Chemistry, Shivaji University, Kolhapur 416004, MS, India

² Department of Chemistry, Balasaheb Desai College, Patan 415206, MS, India

³ Polymer Energy Materials Laboratory, School of Chemical Engineering, Chonnam National University, Gwangju 61186, Republic of Korea

⁴ Optoelectronic Convergence Research Center, School of Chemical Engineering, Chonnam National University, Gwangju 61186, Republic of Korea

⁵ Department of Physics, Shivaji University, Kolhapur 416004, MS, India

* Correspondence: sambhaji_mane@rediffmail.com

Abstract: In the present investigation, a one-step hydrothermal approach is proposed to synthesize Li^+ , Rb^+ , and In^{3+} intercalated $\text{PW}_{12}\text{O}_{40}$ (PTA) thin films. The photoelectrochemical performance of the deposited $\text{Li}_3\text{PW}_{12}\text{O}_{40}$ (Li-PTA), $\text{Rb}_3\text{PW}_{12}\text{O}_{40}$ (Rb-PTA), and $\text{In}_3\text{PW}_{12}\text{O}_{40}$ (In-PTA) photocathodes were investigated using a two-electrode cell configuration of FTO/ $\text{Li}_3\text{PW}_{12}\text{O}_{40}$ /(0.1 M I^-/I^{3-})_{aq.}/Graphite. The energy band gaps of 2.24, 2.11, and 2.13 eV were observed for the Li-PTA, Rb-PTA, and In-PTA films, respectively, as a function of Li^+ , Rb^+ , and In^{3+} . The evolution of the spinal cubic crystal structure with increased crystallite size was observed for Rb^+ intercalation within the PTA Keggin structure, which was confirmed by X-ray diffraction (XRD). Scanning electron microscopy (SEM) revealed a modification in the surface morphology from a rod-like structure to a densely packed, uniform, and interconnected microsphere to small and large-sized microspheres for Li-PTA, Rb-PTA, and In-PTA, respectively. Compositional studies confirmed that the composing elements of Li, Rb, In, P, W, and O ions are well in accordance with their arrangement for Li^+ , Rb^+ , In^{3+} , P^{5+} , W^{6+} , and O^{2-} valence states. Furthermore, the J - V performance of the deposited photocathode shows power conversion efficiencies (PCE) of 1.25%, 3.03%, and 1.62%, as a function of the incorporation of Li^+ , Rb^+ , and In^{3+} ions. This work offers a one-step hydrothermal approach that is a prominent way to develop Li^+ , Rb^+ , and In^{3+} ions intercalated PTA, i.e., $\text{Li}_3\text{PW}_{12}\text{O}_{40}$, $\text{Rb}_3\text{PW}_{12}\text{O}_{40}$, and $\text{In}_3\text{PW}_{12}\text{O}_{40}$ photocathodes for competent solar energy harvesting.

Keywords: polyoxometalates; hydrothermal; phosphotungstate ($\text{PW}_{12}\text{O}_{40}$); thin films; power conversion efficiency (PCE)



Citation: Nadaf, S.N.; Patil, S.S.; Kalantre, V.A.; Mali, S.S.; Patil, J.V.; Hong, C.K.; Patil, S.S.; Bhosale, P.N.; Mane, S.R. Towards Environment Friendly Hydrothermally Synthesized Li^+ , Rb^+ , In^{3+} Intercalated Phosphotungstate ($\text{PW}_{12}\text{O}_{40}$) Thin Films. *Materials* **2023**, *16*, 888. <https://doi.org/10.3390/ma16030888>

Academic Editor: Xunjin Zhu

Received: 13 November 2022

Revised: 8 January 2023

Accepted: 11 January 2023

Published: 17 January 2023



Copyright: © 2023 by the authors. Licensee MDPI, Basel, Switzerland. This article is an open access article distributed under the terms and conditions of the Creative Commons Attribution (CC BY) license (<https://creativecommons.org/licenses/by/4.0/>).

1. Introduction

Due to the limitations of non-renewable energy sources and the consumption of fossil fuels, the development and commercial synthesis of renewable energy sources have piqued the interest of today's scholars in recent years. Because the sun is an infinite source of light energy, researchers are concentrating their efforts on developing new photovoltaic solar cells [1–3]. Polyoxometalates are used in the field of energy, such as solar cells [4] and lithium-ion batteries [5,6]. The most studied Keggin types of structures are $[\text{XM}_{12}\text{O}_{40}]^{n-}$ and $[\text{PMo}_{12}\text{O}_{40}]^{3-}$ [7]. Because these compounds are highly stable in air and water and can conduct reversible and steady electron transfer processes, they are attractive candidates for use in the energy field [8,9]. Although polyoxometalates offer attractive electrochemical characteristics, there have been comparatively few studies of polyoxometalate carried

out on photo-electrochemical solar cells. A photoconversion efficiency (η) of 0.33% was reported in favor of $(\text{PW}_{12}/\text{TiO}_2)_3$ thin films [10], and $\text{PW}_{12-0.75}$ showed the highest (η) of 0.13% [11]. Recently, a Ti^+ -doped phosphomolybdic acid (TIPMA) absorber produced a conversion efficiency of 0.42% [12].

Polyoxometalates (POMs), a well-known class of inorganic nanoclusters with a metal-oxygen framework, have an inherent ability to accept electrons readily [13]. POMs can undergo reversible multielectron redox reactions while retaining their intact structure, making them an efficient electron scavenger to enhance the photoelectrochemical response [14]. Polyoxometalates (POMs), a class of molecular metal-oxo cluster compounds based primarily on Mo, W, and V elements, have demonstrated superior physicochemical properties and a wide range of applications [15,16]. POMs, in particular, have an intrinsic electron acceptor property that is likely to capture photogenerated electrons from the semiconductor conduction band (CB) and thus promote semiconductor power conversion efficiency. Yoon et al. reported that phosphotungstic acid played a vital role in improving the energy conversion efficiency of a TiO_2 anode [17]. Researchers also carried out a systematic study in the fields of conductivity [18], photocatalysts [19,20], semiconductors [21], and polyoxometalates as absorber materials in photovoltaic (PV) cells.

Recently, our group investigated the incorporation of monovalent and trivalent metal ions into POMs films to enhance photoelectrochemical performance. These modifications of POMs upon doping could promote its photoelectrochemical performance; this is a promising strategy for enhancing electron-hole pair recombination, as a result, improving the power conversion efficiency of the PTA photocathode [22,23].

The partial exchange of protons in heteropoly acid with large cations such as Cs^+ , Rb^+ , NH_4^+ , and K^+ transforms a water-soluble acid with a low surface area ($<5 \text{ m}^2\text{g}^{-1}$) into a water-insoluble salt with a surface area greater than $100 \text{ m}^2\text{g}^{-1}$ [24,25]. The presence of the counter cation was discovered to affect the relative stability of heteropoly acids. The heteropolyacids (HPAs) can be altered by exchanging protons with various metal or alkali metal ions. HPA salts are formed by the partial and complete exchange of heteropolyacid protons. As a result, the polyoxometalate materials exhibit significant improvement and optimization in the growth pathway for refining their optoelectronic and photovoltaic properties through the doping strategy. Doping is a technique that involves introducing small amounts of impurities into the lattice of a material, causing changes in the morphological, optostructural, and electrical properties of the parent material [26].

Polyoxometalate Keggin's structure remains intact even after its protons are exchanged with various metal ions. The extent to which protons are exchanged with metal ions has a significant effect on these POMs' photovoltaic, catalytic, and sensing properties. POMs that have been partially exchanged have been reported to have higher acidity than POMs that have been completely exchanged [27]. This is due to the increased surface area, which contributes to the protons' high mobility.

Several research articles on the synthesis of monovalent metal-ion-exchanged polyoxometalate using solid-state ion exchange [28], batch reactor vessels [29], and layer-by-layer methods [30] have been published, but all of these methods produce materials in powder form, which is not suitable for solar cell application in terms of uniformity. Therefore, we have directly implemented the modified one-pot hydrothermal route to synthesize a uniform and adherent thin film, which is a simple and cost-effective procedure.

In the present investigation, the hydrothermal process was directly implemented to construct a $\text{Li}_3\text{PW}_{12}\text{O}_{40}$ (Li-PTA), $\text{Rb}_3\text{PW}_{12}\text{O}_{40}$ (Rb-PTA), and $\text{In}_3\text{PW}_{12}\text{O}_{40}$ (In-PTA) absorber on fluorine-doped tin oxide (FTO) substrates using $\text{Na}_2\text{-EDTA}$ as a complexing agent. The main aim is to investigate the role of dopant monovalent Li^+ , Rb^+ , and trivalent In^{3+} ions in a phosphotungstate anion using a simple one-step hydrothermal process, as well as the effect on optostructural, compositional, and morphological properties. Furthermore, photoelectrochemical properties of directly synthesized $\text{Li}_3\text{PW}_{12}\text{O}_{40}$ (Li-PTA), $\text{Rb}_3\text{PW}_{12}\text{O}_{40}$ (Rb-PTA), and $\text{In}_3\text{PW}_{12}\text{O}_{40}$ (In-PTA) thin films were investigated.

2. Experimental Details

2.1. Chemicals and Material Details

Thin films of Lithium (Li^+), Rubidium (Rb^+), and Indium (In^{3+})-intercalated phosphotungstate anions were synthesized using phosphotungstic acid ($\text{H}_3\text{PW}_{12}\text{O}_{40}$) (PTA) and lithium chloride, rubidium sulfate, and indium sulfate, all of which were purchased from Himedia laboratories and used as sources of $(\text{PW}_{12}\text{O}_{40})^{3-}$ and Li^+ , Rb^+ , and In^{3+} ions, respectively. To allow for the gradual release of cations from the solution, the complex disodium salt of ethylenediaminetetraacetic acid ($\text{Na}_2\text{-EDTA}$, 99.9%, S.D. Fine Chem., Hong Kong, China) was used. An ammonia solution (NH_3 , 25%, Thomas Baker, Mumbai, India) was used to keep the pH of the reaction bath stable. Using an FTO conducting substrate ($\sim 8 \Omega/\text{sq}$, Seoul, Republic of Korea), the photoelectrochemical application of Li^+ , Rb^+ , and In^{3+} -intercalated phosphotungstate anions was investigated. To perform electrochemical reactions, a 0.1 M iodide/polyiodide solution was used to investigate the photoelectrochemical solar cell performance of Li-PTA , Rb-PTA , and In-PTA photoelectrodes. All solutions were produced with double-distilled water (DDW).

2.2. Preparation of Solutions

2.2.1. Phosphotungstic Acid ($\text{H}_3\text{PW}_{12}\text{O}_{40}$)

A 0.02 M $\text{H}_3\text{PW}_{12}\text{O}_{40}$ solution was prepared by dissolving 5.76 g of $\text{H}_3\text{PW}_{12}\text{O}_{40}$ in double-distilled water (DDW) and diluted to 100 mL with DDW.

2.2.2. Lithium Chloride (LiCl)

A 0.1 M LiCl solution was made by dissolving 0.423 g of LiCl in double-distilled water (DDW) and diluting it to 100 mL with DDW.

2.2.3. Rubidium Sulfate (Rb_2SO_4)

The 0.01 M Rb_2SO_4 solution was made by dissolving 0.267 g of Rb_2SO_4 in double-distilled water and diluting it to 100 mL with DDW.

2.2.4. Indium (III) Sulfate ($\text{In}_2(\text{SO}_4)_3$)

To make a 0.1 M $\text{In}_2(\text{SO}_4)_3$ solution, we dissolved 0.517 g of $\text{In}_2(\text{SO}_4)_3$ in double-distilled water and diluted it to 100 mL with DDW.

2.2.5. Ethylene Diamine Tetra Acetic Acid (EDTA)

A 0.1 M EDTA solution was made by dissolving 2.92 g of EDTA in double-distilled water and diluting it to 100 mL with DDW.

2.2.6. Iodide/Polyiodide Electrolyte

Potassium iodide weighing 1.66 g was dissolved in a small amount of distilled water to make a 0.1 M solution. Then 1–2 iodine crystals and a pinch of KCl powder and d were added with double-distilled water to reach 100 mL.

2.3. Synthesis of Li^+ , Rb^+ , In^{3+} Doped PTA Thin Films

The synthesis of Li^+ , Rb^+ , and In^{3+} intercalated PTA thin films was deposited onto the FTO substrate using a one-step hydrothermal route. In the process, the appropriate volume of the 0.02 M $\text{H}_3\text{PW}_{12}\text{O}_{40}$ solution was taken separately, and pH was adjusted to 5.2, 6.8, and 6.5 ± 0.2 for Li^+ , Rb^+ , and In^{3+} , respectively. Using an NH_3 solution, the colored metal-complex reaction solution changed to colorless and was then stirred for 10 min. Subsequently, an appropriate volume of freshly prepared EDTA complexed with a 0.1 M LiCl , $\text{In}_2(\text{SO}_4)_3$, and 0.01 M Rb_2SO_4 salt (Li-EDTA , Rb-EDTA , and In-EDTA) solution was prepared and separately added drop-wise with continuous stirring to the above solution. Finally, the entire reaction mixture was transferred to a 40 mL Teflon-lined steel autoclave, and the precleaned FTO substrate was placed vertically in Teflon with the conducting side facing the solution.

For the hydrothermal synthesis of Li-PTA, Rb-PTA, and In-PTA, the autoclave was stored in the furnace at 90, 85, and 120 ± 2 °C for 3 h. After the desired period, the stainless-steel autoclave was naturally cooled to room temperature and the deposited films were dried for one hour at 100 °C and used for further characterization. Table 1 displays the optimized deposition parameters for Li-PTA, Rb-PTA, and In-PTA thin films.

Table 1. Optimized parameters for the synthesis of Li-PTA, Rb-PTA, and In-PTA thin films.

Sample Code	Bath Composition	pH	Temperature (°C)	Deposition Time (h)
Li-PTA	20 mL of 0.02 M $\text{H}_3\text{PW}_{12}\text{O}_{40}^+$ liquor NH_3^+ 10 mL of Li-EDTA complex were added to the above solution and the whole reaction mixture was put into a Teflon-lined stainless-steel autoclave with a capacity of 40 mL.	5.2 ± 0.2	90 ± 2 °C	3 h
Rb-PTA	20 mL of 0.02 M $\text{H}_3\text{PW}_{12}\text{O}_{40}^+$ liquor NH_3^+ 10 mL of Rb-EDTA complex were added to the above solution and the whole reaction mixture was put into a Teflon-lined stainless-steel autoclave with a capacity of 40 mL.	6.8 ± 0.2	85 ± 2 °C	3 h
In-PTA	20 mL of 0.02 M $\text{H}_3\text{PW}_{12}\text{O}_{40}^+$ liquor NH_3^+ 10 mL of In-EDTA complex were added to the above solution and the whole reaction mixture was put into a Teflon-lined stainless-steel autoclave with a capacity of 40 mL.	6.5 ± 0.2	120 ± 2 °C	3 h

2.4. Characterization of Li-PTA, Rb-PTA, and In-PTA Thin-Film Photocathode

The thickness of the Li-PTA, Rb-PTA, and In-PTA thin films was measured using a surface profilometer (AMBIOS Model-XP-1, Ambios Technology, Milpitas, CA, USA). The optical absorption spectra of the films were measured using a UV-Vis. spectrophotometer (Shimadzu Model-UV-1800, Shimadzu Corporation Analytical & Measuring Instruments Division, Kyoto, Japan) in the 300–700 nm range. An X-ray diffractometer was used to examine the structural properties of Li-PTA, Rb-PTA, and In-PTA films (Bruker Model-140 AXS D8, Bruker Ltd., Mannheim, Germany). Morphology and compositional data of Li-PTA, Rb-PTA, and In-PTA films were investigated using field emission scanning electron microscopy (FE-SEM) (MIRA3 LMH, TESCAN, Brno, Czech Republic, EU) coupled with energy-dispersive spectroscopy (EDS) (JEOL-JSM 6360A, JEOL Ltd., Tokyo, Japan). The analysis of valence states of constituted ions present in the Li-PTA, Rb-PTA, and In-PTA films was performed with X-ray photoelectron spectroscopy (XPS, Thermo Scientific, Model: Multilab-2000, Waltham, MA, USA).

A simple two-electrode cell configuration system was used to investigate the photo-electrochemical cell performance of Li-PTA, Rb-PTA, and In-PTA photocathodes. In the photo-electrochemical cell (PEC) setup, deposited Li-PTA, Rb-PTA, and In-PTA thin films serve as a photocathode, while the graphite plates serve as counter electrodes in a 0.1 M Iodide/polyiodide redox electrolyte solution under dark and light illumination from a 500 W tungsten lamp (light intensity of 100 mW/cm²). The electrode cell configuration of FTO/Rb-PTA | (0.1 M Iodide/polyiodide)_{aq.} | Graphite was used to assess the PEC performance. The spacing between the photocathode and the counter electrode was sustained up to ~1 cm. The electrochemical measurements were performed on an Autolab electrochemical workstation using NOVA software (Model: Autolab, PGSTAT 100 potentiostat, Metrohm, Herisau, Switzerland).

3. Results and Discussion

3.1. Proposed Growth and Reaction Pathway for Li-PTA, Rb-PTA, and In-PTA Thin Films

The surface morphology and crystal quality of Li-PTA, Rb-PTA, and In-PTA thin films depend on the deposition process of the films onto the substrate. A simple and easy low-cost hydrothermal approach is employing Na₂-EDTA as a complexing agent to deposit Li-PTA, Rb-PTA, and In-PTA films onto a conducting fluorine-doped tin oxide (FTO) substrate. In this, the different metal ions were complexed with Na₂-EDTA. Herein, the controlled release of metal ions at an optimized temperature and pressure is the reason for the chelating agent in this reaction. The Na₂-EDTA is a useful organic complexing agent that helps to deposit high-quality Li-PTA, Rb-PTA, and In-PTA thin films by allowing different metal ions such as Lithium (Li⁺), Rubidium (Rb⁺), and (Indium) In³⁺ to slowly escape during the deposition process.

We controlled the deposition parameters of Li-PTA, Rb-PTA, and In-PTA films such as the temperature, pH, and precursor concentration to allow slowly released Li⁺, Rb⁺, and In³⁺ metal ions to react with phosphotungstate (PW₁₂O₄₀)³⁻ ions. The optimized temperature and pressure in the hydrothermal reaction promote a rapid rate of reaction by supplying heat energy to the reactant. As a result, a white-colored precipitate forms rather than a film. To avoid precipitation, metal ions are complexed with Na₂-EDTA and decrease the precipitate with the formation of Li₃PW₁₂O₄₀, Rb₃PW₁₂O₄₀, and In₃PW₁₂O₄₀ in powder form. At an optimized temperature and pressure, metal ions Li⁺, Rb⁺, and In³⁺ slowly dissociate from Li-EDTA, Rb-EDTA, and In-EDTA complexes inside the reaction and are deposited via ion-by-ion condensation followed by the Ostwald ripening process. In optimum conditions, smaller, thermodynamically unstable nuclei join one another to produce bigger stable crystals, according to the Ostwald ripening law [31]. When the ionic products of Li⁺, Rb⁺, and In³⁺ and (PMo₁₂O₄₀)³⁻ ions progress to the solubility product of the Li₃PW₁₂O₄₀, Rb₃PW₁₂O₄₀, and In₃PW₁₂O₄₀ thin films, the deposition of Li-PTA, Rb-PTA, and In-PTA thin films on the conducting FTO substrate occur [32].

Hydrothermally synthesized Li₃PW₁₂O₄₀, Rb₃PW₁₂O₄₀, and In₃PW₁₂O₄₀-based thin films exhibit good optoelectronic properties with Li⁺, Rb⁺, and In³⁺ intercalation, resulting in uniform, adherent, and improved film quality. The possible growth mechanism for the deposition of (i) Li-PTA, (ii) Rb-PTA, and (iii) In-PTA films by a cost-effective, simple, one-step hydrothermal technique is shown in Figure 1.

(i) The reaction pathway for the deposition of Li₃PW₁₂O₄₀ films is as follows:

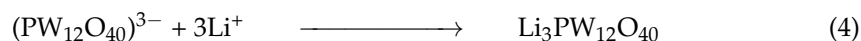
Initially, the formation of metal ion complex Li₂-EDTA in an aqueous medium is demonstrated in reaction (1)



At an optimal pH and reaction temperature, the H₃PW₁₂O₄₀ and Li₂-EDTA complex dissociated and formed (PW₁₂O₄₀)³⁻ and Li⁺, respectively, as shown in reactions (2) and (3) below.



When ionic products of Li⁺ and (PW₁₂O₄₀)³⁻ ions exceeded and formed Li-PTA as a solubility product, the formation of a Li₃PW₁₂O₄₀ film onto the FTO substrate was demonstrated in reaction (4).

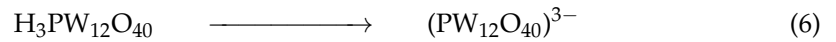


(ii) The reaction pathway for the formation of Rb₃PW₁₂O₄₀ films is as follows.

As demonstrated in reaction (5), the $\text{Rb}_2\text{-EDTA}$ complex is formed in an aqueous medium.



At an optimized pH and reaction temperature, the $\text{H}_3\text{PW}_{12}\text{O}_{40}$ and $\text{Rb}_2\text{-EDTA}$ complex dissociated and formed $(\text{PW}_{12}\text{O}_{40})^{3-}$ and Rb^+ , respectively, as shown in reactions (6) and (7) below.



When ionic products of Rb^+ and $(\text{PW}_{12}\text{O}_{40})^{3-}$ ions exceeded and formed Rb-PTA as a solubility product, reaction (8) demonstrates the formation of the $\text{Rb}_3\text{PW}_{12}\text{O}_{40}$ thin film on the FTO substrate.

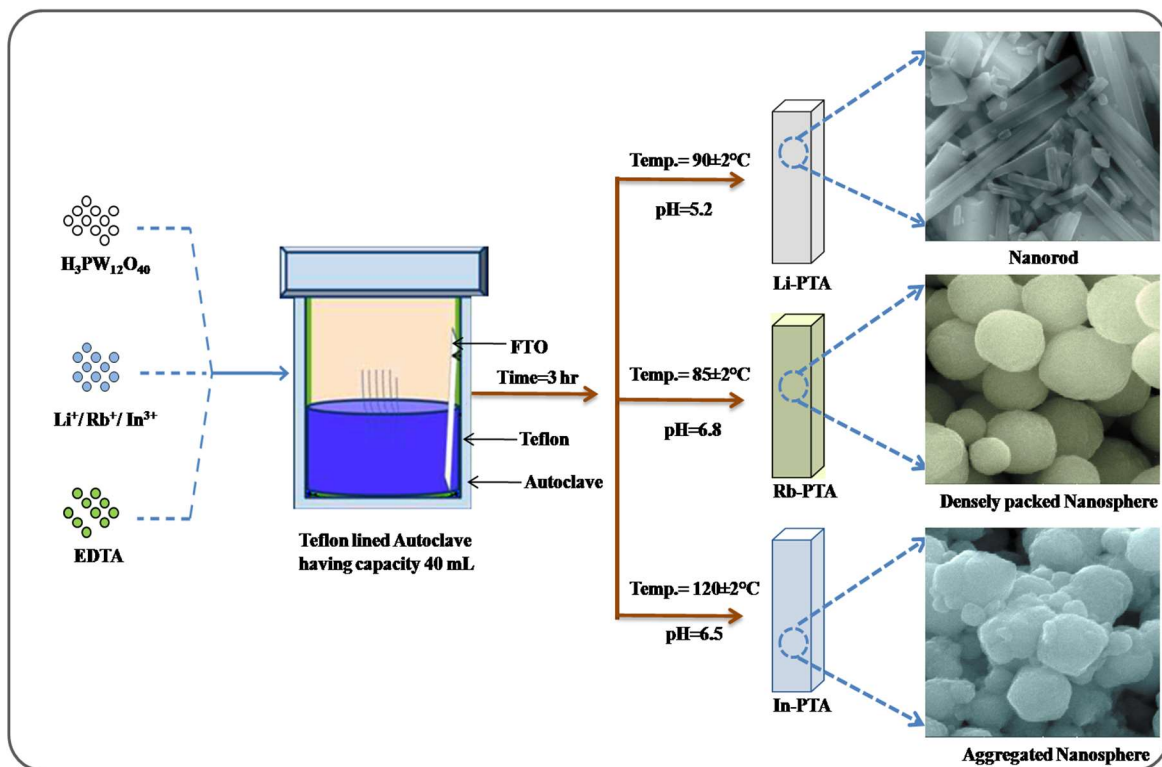
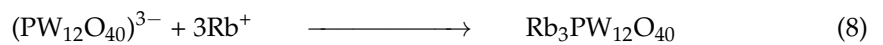
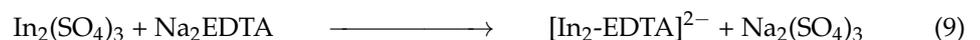


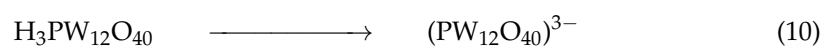
Figure 1. Graphical representation of possible growth mechanism of (i) $\text{Li}_3\text{PW}_{12}\text{O}_{40}$, (ii) $\text{Rb}_3\text{PW}_{12}\text{O}_{40}$, and (iii) $\text{In}_3\text{PW}_{12}\text{O}_{40}$ thin film deposited by the single-step hydrothermal approach.

(iii) The reaction pathway for the formation of $\text{In}_3\text{PW}_{12}\text{O}_{40}$ films is as follows.

The formation of an $\text{In}_2\text{-EDTA}$ complex in an aqueous medium is demonstrated in reaction (9).



At an optimized pH and reaction temperature, the $\text{H}_3\text{PW}_{12}\text{O}_{40}$ and $\text{In}_2\text{-EDTA}$ complex dissociated and formed $(\text{PW}_{12}\text{O}_{40})^{3-}$ and In^{3+} , respectively, as shown in reactions (10) and (11) below.





When ionic products of In^{3+} and $(\text{PW}_{12}\text{O}_{40})^{3-}$ ions exceeded and formed In-PTA as a solubility product, this resulted in the formation of $\text{In}_3\text{PW}_{12}\text{O}_{40}$ thin film on the FTO substrate as indicated in reaction (12).



3.2. Thickness Studies

A surface profilometer was used to calculate the thickness of the as-deposited Li-PTA, Rb-PTA, and In-PTA thin films, which were found to be 510, 620, and 570 nm, respectively. The thickness of the deposited films is controlled by uniform growth and surface morphology.

3.3. Optical Absorption Studies

The film thickness of Li-PTA, Rb-PTA, and In-PTA films plays a crucial role in optical absorption studies, which are found to be 510, 620, and 570 nm, respectively. The synthesized Li-PTA, Rb-PTA, and In-PTA thin films indicate maximal light absorption within the range of 500–600 nm, which is observed in Figure 2a; as seen from the absorption spectra, slight shifting was observed in the absorption edge from Li^+ to In^{3+} to Rb^+ intercalation in the PTA film. The energy band gap of the Li-PTA, Rb-PTA, and In-PTA thin films decreases with an increase in thickness. Large-sized cations intercalate in $\text{PW}_{12}\text{O}_{40}$, increasing the grain-size expansion of Li-PTA, Rb-PTA, and In-PTA, which help to shrink the voids, leading to Li-PTA, Rb-PTA, and In-PTA absorbers. Furthermore, the decrease in band-gap energy of $\text{PW}_{12}\text{O}_{40}$ thin films might be due to additional energy levels introduced by Li^+ , Rb^+ , and In^{3+} ions, which are close to the valence band edge in the E_g of the host $\text{PW}_{12}\text{O}_{40}$, or a decrease in the energy associated with the direct and allowed transition, which causes the position of the absorption edge to shift to higher wavelength [33–36]. The band gap of deposited Li-PTA, Rb-PTA, and In-PTA films was determined by plotting the graph of $(\alpha hv)^2$ versus (hv) , as shown in Figure 2b–d, which depends on Tauc Equation (13) [37].

$$\alpha = \frac{A(hv - E_g)^n}{hv} \quad (13)$$

In which, ' h ' is Planck's constant, ' E_g ' is the thin-film energy bandgap, exponent ' n ' is the type of electronic transition, and ' A ' is the parameter that depends on the probability of the electronic transition.

The optical absorption spectra of thin films have been studied to determine the absorption coefficient and optical energy gap. The optical properties of thin films are affected by their thickness and the chemical elements or compounds that comprise them. Photovoltaic, optoelectronics, electrochromic performance, solar cells, and photo-electrochemistry are some applications based on the optical absorption of thin films. Absorption is proportional to both the thickness of the film samples and the concentration of the absorbing material [26].

The calculated band gaps for Li-PTA, Rb-PTA, and In-PTA films were 2.24, 2.11, and 2.13 eV, respectively, as a result of Li^+ , In^{3+} , and Rb^+ ions intercalated in the PTA, which is lower than the parent PTA (3.24 eV). The energy band gap decreased owing to the increased thickness of Li-PTA, Rb-PTA, and In-PTA films. Moreover, a reduced band gap was observed in the PTA after Rb^+ intercalation compared to Li^+ and In^{3+} , which is attributed to the increased thickness of synthesized films and the improved grain size. As a result, a densely packed and well-grown $\text{Rb}_3\text{PW}_{12}\text{O}_{40}$ nanosphere film was formed. Rb-PTA has a narrower band gap than Li-PTA and In-PTA, which increases light absorption in photoelectrochemical cells [38].

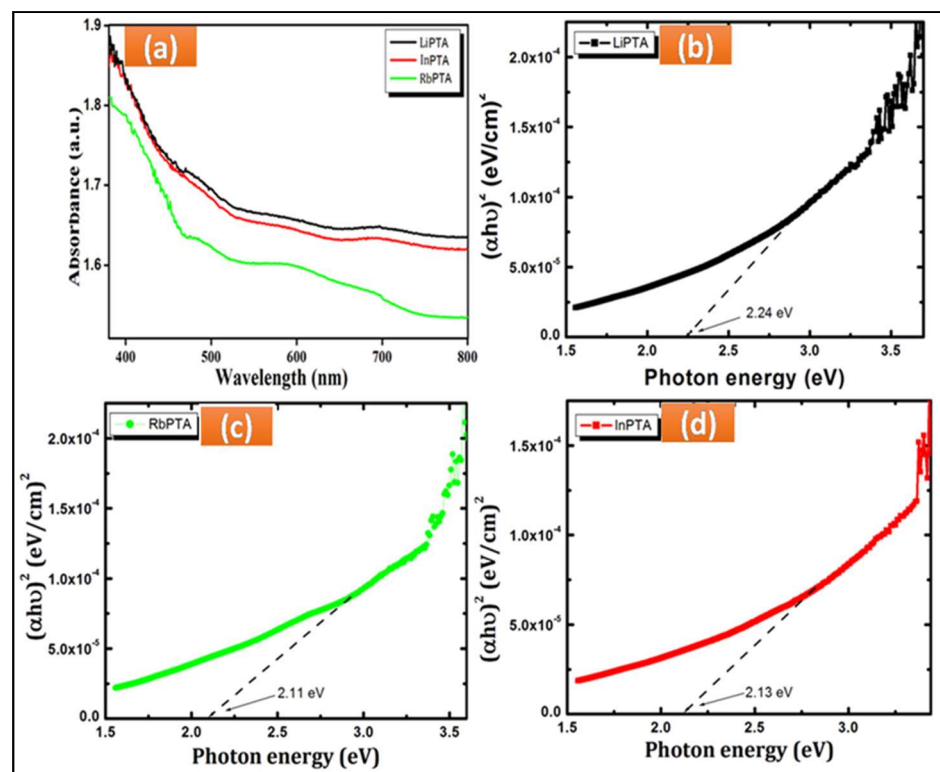


Figure 2. (a) Optical absorption spectra for Li-PTA, Rb-PTA, and In-PTA thin films and optical band gap of (b) Li-PTA (c) Rb-PTA, and (d) In-PTA thin films.

3.4. Structural Analysis of Li-PTA, Rb-PTA, and In-PTA by XRD

The crystal structures of synthesized Li^+ , Rb^+ , and In^{3+} -intercalated PTA films were assessed by the XRD patterns. The XRD analysis of synthesized Li-PTA, Rb-PTA, and In-PTA films were shown in Figure 3. As seen from Figure 3, the Li-PTA, Rb-PTA, and In-PTA films all show similar X-ray diffractograms of the body-centered cubic secondary Kegglin structure with major diffraction peaks at 10.50 – 10.80 , 15.15 – 15.32 , 18.45 – 18.70 , 21.27 – 21.53 , 26.41 – 26.69 , 30.59 – 30.85 , 36.00 – 36.27 , and 39.20 – 39.35° [39]. Compared to pure PTA, a slight shift in the prominent plane (222) towards higher 2θ values was observed in Li-PTA, Rb-PTA, and In-PTA, indicating the successful intercalation of Li^+ , Rb^+ , and In^{3+} in PTA. It is presumed that the Li^+ , Rb^+ , and In^{3+} -intercalated PTA show similar symmetry but contracted unit cells.

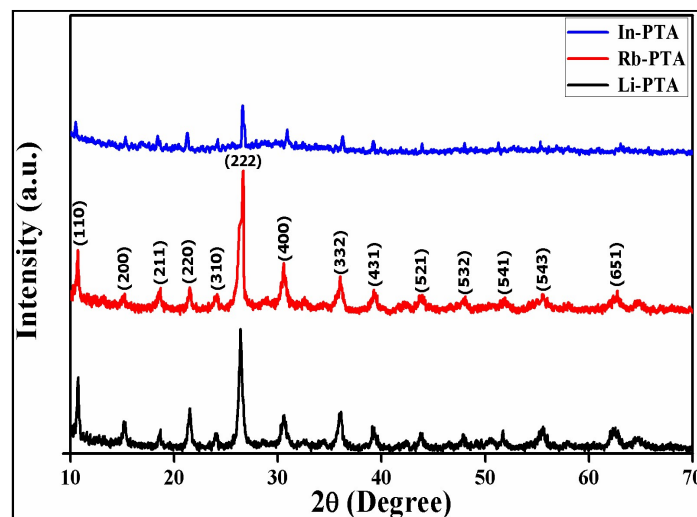


Figure 3. XRD patterns of Li-PTA, Rb-PTA, and In-PTA thin films.

The lattice parameters for the spinel cubic structure ($a=b=c$) for Li^+ , Rb^+ , and In^{3+} -intercalated PTA were found to be 12.02, 11.52, and 11.90 Å, respectively [29,40]. This shrinkage of the unit cell can be described by the exchangeable protons present in the secondary Keggin structure in the form of dihydronium ions H_5O_2^+ for hydrated Li^+ , Rb^+ , and In^{3+} cations, which are primarily responsible for the contraction in the unit cell parameter. This type of behavior was observed by Borghese et al. [41]. As a result, XRD demonstrates the successful intercalation of Li^+ , Rb^+ , and In^{3+} ions into PTA while preserving the Keggin structure. We calculated the crystallite size for Li-PTA, Rb-PTA, and In-PTA samples using Scherrer's Equation (14) [42].

$$D = \frac{0.94 \lambda}{\beta \cos \theta} \quad (14)$$

where 'D' is the crystallite size (nm), ' λ ' is the radiation source ($\text{CuK}\alpha = 1.5406 \text{ \AA}$), ' β ' is the full width at half maximum (FWHM) intensity (taken in radians), and ' θ ' is Bragg's diffraction angle (degree).

As shown in Table 2, the calculated crystallite sizes for Li-PTA, Rb-PTA, and In-PTA were 48.85, 72.03, and 52.54 nm, respectively. The larger rubidium cation size can be attributed to the increased crystallite size observed on Rb^+ intercalated within the PTA Keggin structure. When metal ions intercalate, the reaction accelerates, resulting in the creation of a large number of nuclei and, as a result, a larger crystallite size, which is beneficial for lowering electron-hole pair recombination [26,31]. Crystallite-size-dependent structural parameters such as the dislocation density (δ) and microstrain (ϵ) were assessed using Equations (15) and (16) [43].

$$\delta = \frac{1}{D^2} \quad (15)$$

$$\epsilon = \frac{\beta \cos \theta}{4} \quad (16)$$

Table 2. Structural parameters of Li-PTA, Rb-PTA, and In-PTA thin films.

Sample Code	Crystallite Size (nm)	Dislocation Density (δ) (Line m^{-2}) $\times 10^{14}$	Microstrain (ϵ) ($\text{line}^{-2} \text{ m}^{-4}$) $\times 10^{-4}$	Experimental d-Spacing Value (Å)
Li-PTA	48.85	3.71	6.68	3.36
Rb-PTA	72.03	1.92	4.81	3.33
In-PTA	52.54	3.27	5.96	3.34

It is clearly shown that crystallite size was increased in the Rb-PTA thin film compared to Li-PTA and In-PTA thin films due to the improved crystal quality and decreased recombination rate between the electrons and holes, resulting in increased J_{sc} and V_{oc} values and subsequently increased photoelectrochemical performance. Dislocation density (δ) and microstrain (ϵ) were calculated using Equations (15) and (16) and presented in Table 2. The estimated XRD parameters were correlated with the reported data. Furthermore, XRD analysis revealed that the Rb-PTA thin film has improved crystallinity when compared to Li-PTA and In-PTA thin films, lowering the grain boundary resistance and defect levels in Rb-PTA thin film. A reduced grain boundary in an Rb-PTA photocathode was beneficial for increasing power conversion efficiency.

3.5. Morphological Studies

The influence of Li^+ , Rb^+ , and In^{3+} ions on the surface morphology of PTA thin films was investigated using scanning electron microscopy (SEM). Figure 4a-f indicates SEM images of Li-PTA, Rb-PTA, and In-PTA samples at low and high magnifications. Figure 4a,b show low- and high-magnification SEM photographs of the Li-PTA film with irregular-sized rod-like structures and an average grain size of ~ 0.08 – $0.32 \mu\text{m}$. Low- and

high-magnification SEM pictures of the Rb–PTA thin film confirm the formation of a densely packed, well-grown, uniform-sized and -shaped, interconnected, microspherical surface morphology with an average grain size of $\sim 0.50\text{--}0.70\ \mu\text{m}$, as shown in Figure 4c,d. Figure 4e,f show low- and high-magnification SEM pictures of the In–PTA thin film and reveal the creation of small and large-sized micro-spherical surface morphology with an average grain size of $\sim 0.35\text{--}0.60\ \mu\text{m}$, respectively.

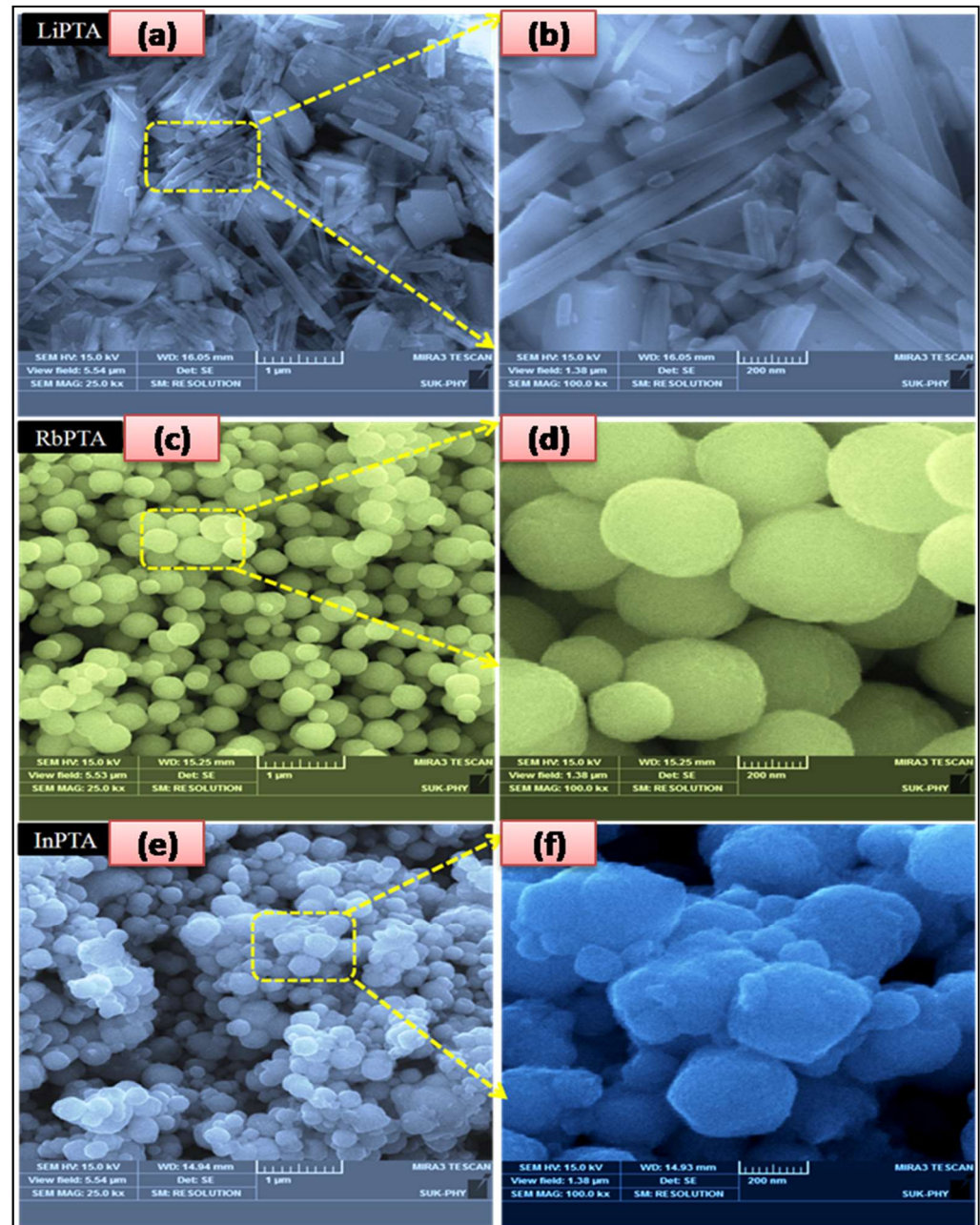


Figure 4. Low- and high-magnification SEM photographs of (a,b) Li–PTA, (c,d) Rb–PTA, and (e,f) In–PTA thin films.

Hydrothermally produced microsphere and rod-shaped surface morphologies are significant for improving optical, electrical, and electronic properties, as well as increasing the surface area for light absorption in solar cells. Overall, the morphological analysis shows that developing the Rb–PTA surface morphology with interconnected microspheres

of increasing grain size, which reduces grain boundary resistance, is useful for the further enhancement of electrochemical properties [39].

3.6. Compositional Studies

The chemical composition of the Li^+ , Rb^+ , and In^{3+} ion-doped phosphotungstate anion influences the output of PEC performance because it reveals the stoichiometry of the produced Li-PTA, Rb-PTA, and In-PTA photocathodes, hence EDAX analysis is performed for Li-PTA, Rb-PTA, and In-PTA. Figure 5a–c depict the elemental composition of constituent elements present in Li-PTA, Rb-PTA, and In-PTA thin films, respectively. The EDAX spectra of the deposited Li-PTA thin film are shown in Figure 5a, and the peaks that arise at binding energies (B.E.) of 0.5, 2.1, and 1.4 KeV confirm the presence of oxygen, phosphorus, and tungsten elements, respectively. Lithium has the atomic number of ($Z = 3$) and it has very low energy and is not detected in EDAX analysis due to the detection limit. The EDAX spectra of the deposited Rb-PTA thin film are shown in Figure 5b. Peaks confirm the existence of oxygen, phosphorus, tungsten, and rubidium elements at 0.5, 2.1, 1.4, and 1.8 KeV binding energies, respectively. Figure 5c depicts the EDAX spectra of the deposited In-PTA thin film. The peaks appear at binding energies of 0.5, 2.1, 1.4, and 3.3 KeV, which validate the occurrence of oxygen, phosphorus, tungsten, and indium, respectively. The EDAX analysis indicates that theoretical and experimental atomic percentages of Li-PTA, Rb-PTA, and In-PTA samples are consistent, tabulated in the right inset of Figure 5a–c [44]. Distinct atomic percentages of O, P, and W were observed in deposition; this is due to the reactivity of monovalent and trivalent ions to bare $\text{PW}_{12}\text{O}_{40}$.

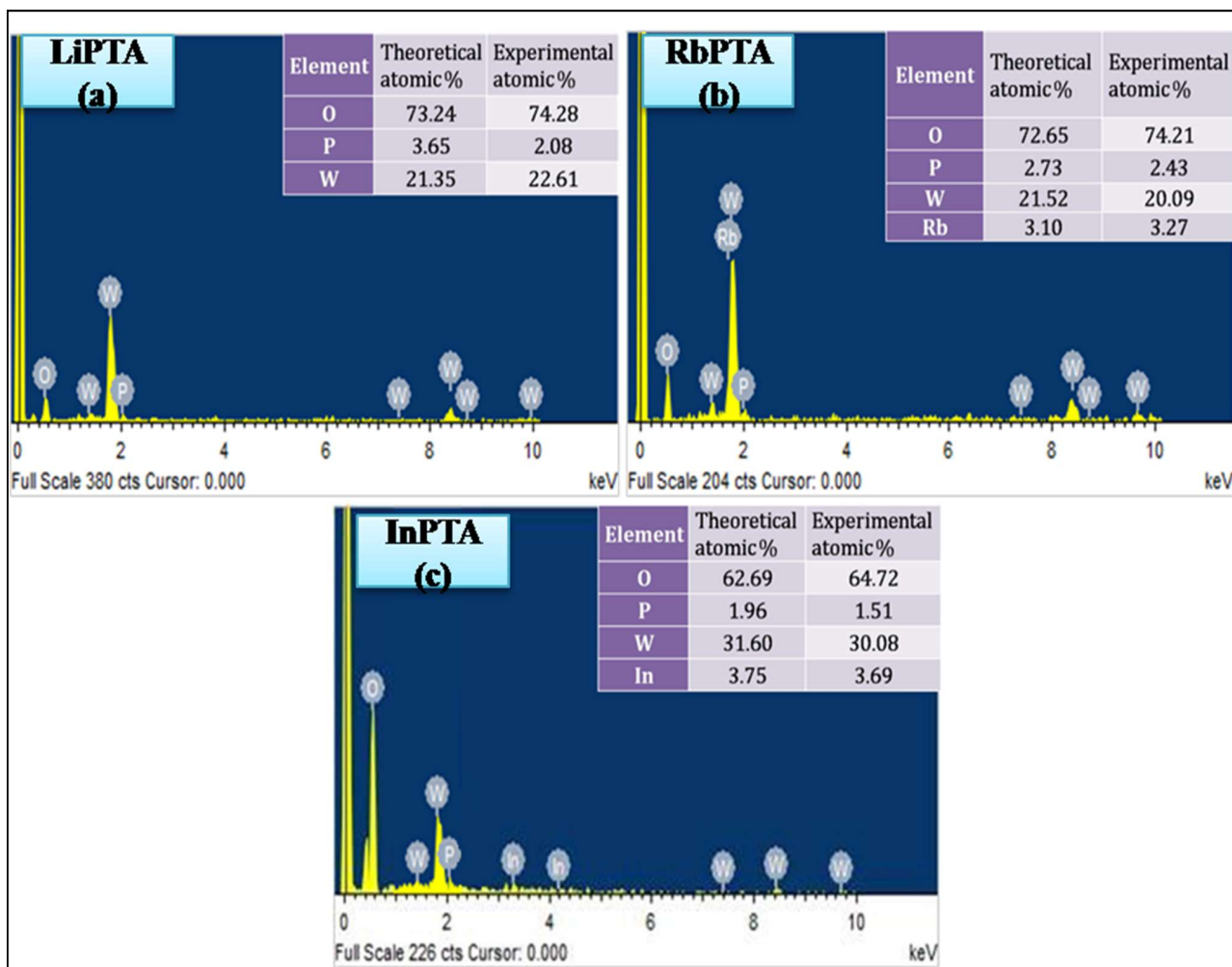


Figure 5. Energy-dispersive X-ray spectra of (a) Li-PTA, (b) Rb-PTA, and (c) In-PTA thin films.

Figure 6 shows the XPS analyses of Li-PTA, Rb-PTA, and In-PTA films that were analyzed to investigate the chemical parameters of the $\text{Li}_3\text{PW}_{12}\text{O}_{40}$, $\text{Rb}_3\text{PW}_{12}\text{O}_{40}$, and $\text{In}_3\text{PW}_{12}\text{O}_{40}$ thin films. Figure 6a demonstrates the XPS survey spectrum of the Li-PTA sample, which shows the occurrence of Li, P, W, and O elements with their corresponding binding energy (B.E.) positions, which confirms the presence of lithium (1+), phosphorus (5+), tungsten (6+), and oxygen (2-) oxidation states. Figure 6b represents the XPS survey spectrum of the Rb-PTA sample, which shows the existence of Rb, P, W, and O elements with their respective binding energies positions, which confirms the presence of rubidium (1+), phosphorus (5+), tungsten (6+), and oxygen (2-) oxidation states. Figure 6c depicts the XPS survey spectrum of the In-PTA sample, which affirms the presence of In, P, W, and O elements with their corresponding (B.E.) positions, which confirms the presence of indium (3+), phosphorus (5+), tungsten (6+), and oxygen (2-) oxidation states. In addition, the survey spectra of Li-PTA, Rb-PTA, and In-PTA contain a carbon peak, which is assigned as adventitious carbon.

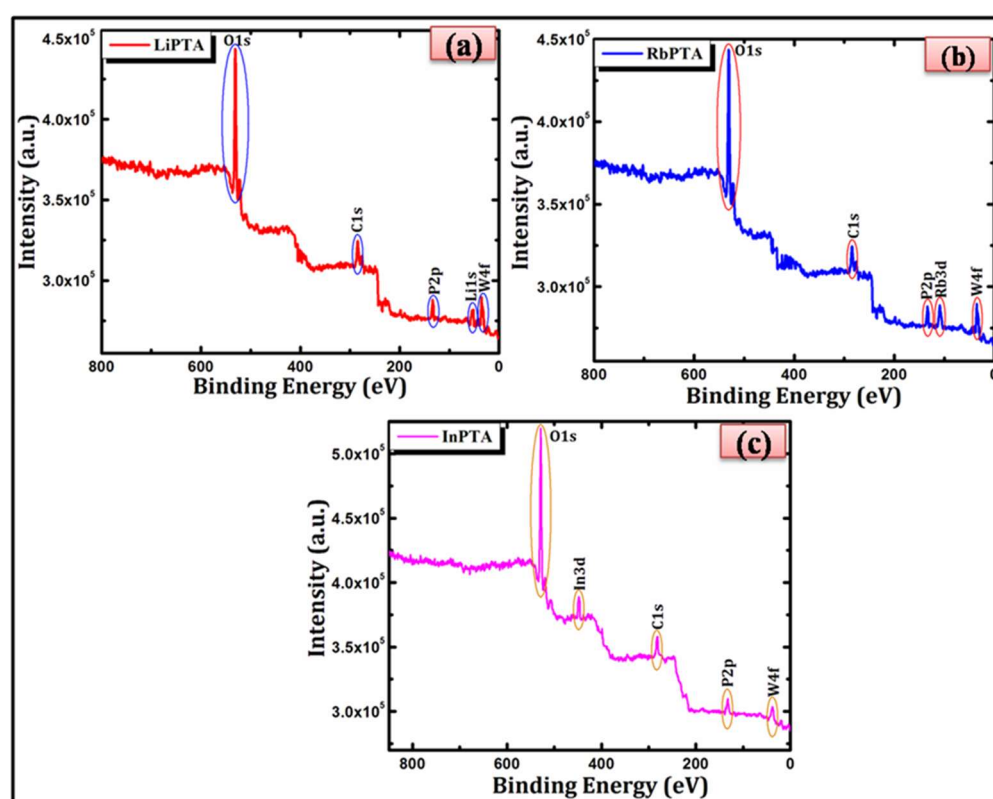


Figure 6. XPS survey spectra of (a) Li-PTA, (b) Rb-PTA, and (c) In-PTA thin films.

Overall, the survey spectra for Li-PTA, Rb-PTA, and In-PTA -based thin films show they are composed of elements Li, Rb, In, P, W, and O ions are reliable in their arrangement for Li^+ , Rb^+ , In^{3+} , P^{5+} , W^{6+} , and O^{2-} valence states, confirming that synthesized Li-PTA, Rb-PTA, and In-PTA thin films are consistent with their stoichiometric formula, $\text{Li}_3\text{PW}_{12}\text{O}_{40}$, $\text{Rb}_3\text{PW}_{12}\text{O}_{40}$, and $\text{In}_3\text{PW}_{12}\text{O}_{40}$, respectively.

3.7. Photoelectrochemical Performance of Li-PTA, Rb-PTA, and In-PTA Thin Films

The photoelectrochemical performance of Li-PTA, Rb-PTA, and In-PTA photocathodes was measured with a simple, cost-efficient, liquid junction photoelectrochemical (PEC) cell. Figure 7 depicts a schematic illustration of the Rb-PTA photocathode in the PEC cell configuration. The photoelectrodes in the PEC cells were made up of Li-PTA, Rb-PTA, and In-PTA thin films. A graphite blade acted as a counter electrode, and an electrolyte solution of 0.1 M Iodide/polyiodide was utilized for the electrochemical pro-

cess. The photoelectrochemical cell is represented as:FTO/Rb-PTA | Iodide/polyiodide (0.1 M) | Graphite.

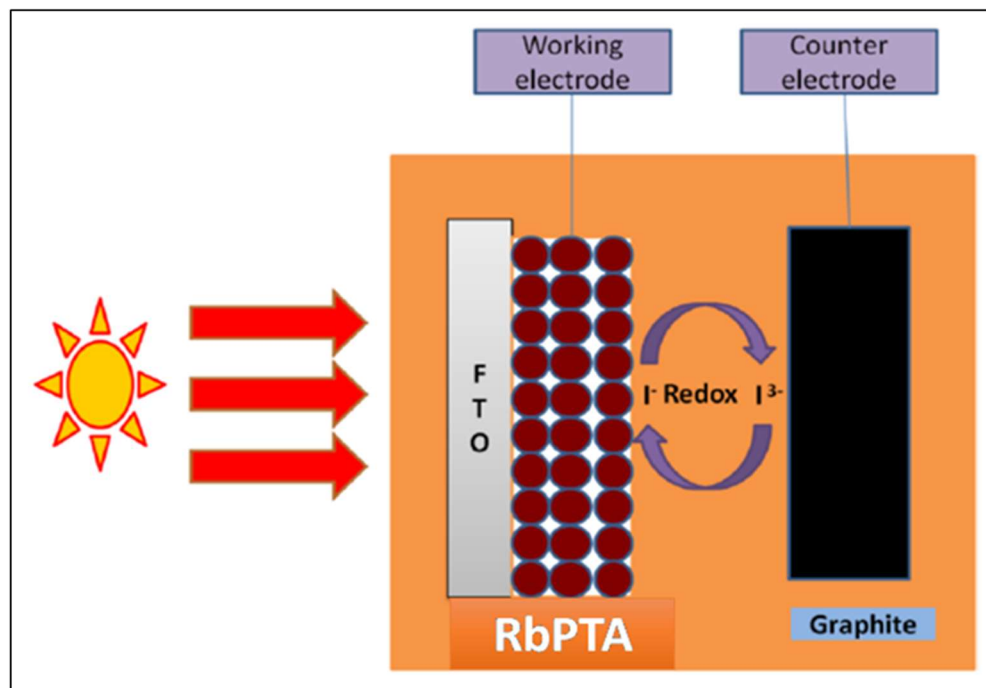


Figure 7. Schematic representation of Rb-PTA photocathode.

The *J-V* characteristics of the Li-PTA, Rb-PTA, and In-PTA photocathodes were analyzed on the auto-lab electrochemical workstation shown in Figure 8a–c. When the photocathode was exposed to light, it absorbed incident light. As a result, an electronic transition appeared from the valence band (VB) to the conduction band (CB). Current density–voltage measurements were performed on deposited Li-PTA, Rb-PTA, and In-PTA samples without and with illumination from a 100 mW/cm² filament lamp. Figure 8 shows that, under dark conditions, Li-PTA, Rb-PTA, and In-PTA photoelectrodes behave similarly to rectifier diodes, and under light irradiation, it is observed that the magnitude of the open-circuit voltage increases with positive polarity, confirming that Li-PTA, Rb-PTA, and In-PTA photoelectrodes are *p*-type semiconductors.

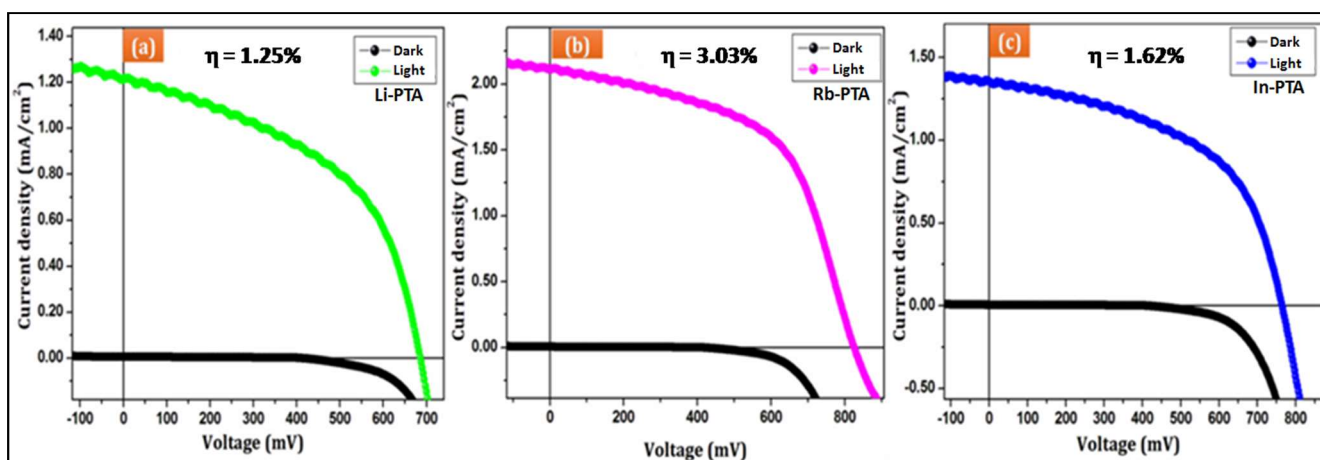


Figure 8. Current density–voltage (*J-V*) characteristics of deposited (a) Li-PTA, (b) Rb-PTA, and (c) In-PTA.

From the J - V curves, the fill factor (FF) and power conversion efficiency ($\eta\%$) of Li^+ , Rb^+ , and In^{3+} -intercalated PTA films were evaluated using Equations (17) and (18) [45].

$$FF = \frac{J_{max} \times V_{max}}{J_{sc} \times V_{oc}} \quad (17)$$

$$\eta\% = \frac{J_{sc} \times V_{oc}}{P_{in}} \times FF \times 100 \quad (18)$$

where ' J_{max} ' is the maximum output current, ' V_{max} ' is the maximum output voltage, ' J_{sc} ' is the short-circuit current, ' V_{oc} ' is the open circuit voltage, and ' P_{in} ' is the input light intensity of a tungsten lamp (100 mW/cm^2).

As seen from the J - V analysis, there was an increment in current density upon Li^+ , Rb^+ , and In^{3+} -intercalated PTA films. The calculated power conversion efficiency for Li -PTA, Rb -PTA, and In -PTA was 1.25%, 3.03%, and 1.62%, respectively. An improvement in PEC was seen due to the intercalation of Li^+ , Rb^+ , and In^{3+} in PTA. Table 3 summarizes all of the photo-electrochemical cell performance data, which shows lower V_{oc} values observed in the J - V measurements. This might be due to recombination processes in the photoelectrochemical cell [46,47].

Table 3. Photoelectrochemical parameters of Li -PTA, Rb -PTA, and In -PTA photocathode.

Sample Code	E_g (eV)	J_{sc} (mA cm^{-2})	V_{oc} (mV)	J_{max} (mA cm^{-2})	V_{max} (mV)	FF	$\eta\%$
Li -PTA	2.24	1.23	690	0.92	418	0.44	1.254
Rb -PTA	2.11	2.20	827	1.67	571	0.50	3.032
In -PTA	2.13	1.35	770	1.05	465	0.46	1.627

As seen from Figure 8, when Li^+ , Rb^+ , and In^{3+} were intercalated in PTA, an increase in current density and open-circuit voltage was seen as a result of improving the PEC performance. The increase in PEC output is due to the formation of compactly and densely packed uniform films of Li -PTA, Rb -PTA, and In -PTA, respectively. Rb -PTA presents highly uniform and compact film formation that reduces the number of grain boundaries and provides enough space to absorb photons compared to Li -PTA and In -PTA thin films. Furthermore, the uniform film surface shows close exposure between the electrolyte the and electrode along with a sufficient surface area for photogenerated electrons, while the less uniform film is present in Li -PTA and In -PTA, which licks the photocurrent, thus forming a low current that accomplishes the lower conversion efficiency as compared to Rb -PTA. Overall, the Rb -PTA photocathode exhibits a better photoelectrochemical performance, attributed to improvements in the densely packed film and increased thickness, providing enough surface for solar energy absorption and diminishing the rate of electron-hole pair recombination, which is useful for photoabsorption in photoelectrochemical solar cells.

4. Conclusions

To fabricate the Li -PTA, Rb -PTA, and In -PTA thin films onto FTO substrates, a one-step, cost-effective, non-toxic hydrothermal route was used. Optical and structural studies revealed that Rb -PTA thin films exhibit direct and appropriate types of transitions with lower energy bandgap, i.e., 2.11 eV, when compared to Li -PTA and In -PTA thin films. The surface morphology of Li^+ , Rb^+ , and In^{3+} intercalation in PTA differs, resulting in irregular rods, interconnected microspheres, and agglomerated microspheres, respectively. The presence of Li , Rb , In , P , W , and O ions with valence states of Li^+ , Rb^+ , In^{3+} , P^{5+} , W^{6+} , and O^{2-} is confirmed by compositional data. The PEC study confirms the generation of conversion efficiencies of 1.25%, 3.03%, and 1.62% for Li -PTA, Rb -PTA, and In -PTA photocathodes, respectively. Improvement in the power conversion efficiency (PCE) for Rb -PTA was observed, attributed to the optimal bandgap produced after Rb^+ ion interca-

lation. Moreover, from the achieved results, the one-step hydrothermal approach is a better alternative than other thin-film deposition techniques.

Author Contributions: Software, C.K.H.; Formal analysis, S.S.P. (Sharadchandra S. Patil); Investigation, P.N.B. and S.R.M.; Writing—original draft, S.N.N.; Writing—review & editing, S.S.P. (Satish S. Patil); Supervision, S.S.M., J.V.P. and S.R.M.; Project administration, V.A.K. All authors have read and agreed to the published version of the manuscript.

Funding: This research received no external funding.

Institutional Review Board Statement: Not applicable.

Informed Consent Statement: Not applicable.

Data Availability Statement: Not applicable.

Acknowledgments: One of the authors, Sameer N. Nadaf, is thankful to the Shri Venkateshwara College of Science, Peth, the Nanasaheb Mahadik College of Engineering, Peth, K.R.P Kanya Mahavidyalaya Islampur, Balasaheb Desai College, Patan, and Materials Research Laboratory, Department of Chemistry, Shivaji University, Kolhapur for providing lab facility.

Conflicts of Interest: The authors announce that they have no conflict of interest.

References

1. Badkooobehzaveh, A.M.; Abdizadeh, H.; Golobostanfard, M.R. Electrophoretic behavior of solvothermal synthesized anion replaced $\text{Cu}_2\text{ZnSn}(\text{S}_x\text{Se}_{1-x})_4$ films for photoelectrochemical water splitting. *Int. J. Hydrogen Energy* **2018**, *43*, 11990. [CrossRef]
2. Kim, K.J.; Pan, C.; Bansal, S.; Malhotra, R.; Kim, D.; Chang, C. Scalably synthesized environmentally benign, aqueous-based binary nanoparticle inks for $\text{Cu}_2\text{ZnSn}(\text{S},\text{Se})_4$ photovoltaic cells achieving over 9% efficiency. *Sustain. Energy Fuels* **2017**, *1*, 267. [CrossRef]
3. Tiwari, D.; Skidchenko, E.; Bowers, J.; Yakushev, M.; Martin, R.; Fermin, D.J. Spectroscopic and electrical signatures of acceptor states in solution processed $\text{Cu}_2\text{ZnSn}(\text{S},\text{Se})_4$ solar cells. *J. Mater. Chem. C* **2017**, *5*, 12720. [CrossRef]
4. Palilis, L.C.; Vasilopoulou, M.; Douvas, A.M.; Georgiadou, D.G.; Kennou, S.; Stathopoulos, N.A.; Constantoudis, V.; Argitis, P. Solution processable tungsten polyoxometalate as highly effective cathode interlayer for improved efficiency and stability polymer solar cells. *Sol. Energy Mater. Sol. Cells* **2013**, *114*, 205. [CrossRef]
5. Uematsu, S.; Quan, Z.; Suganuma, Y.; Sonoyama, N. Reversible lithium charge–discharge property of bi-capped Keggin-type polyoxovanadates. *J. Power Sources* **2012**, *217*, 13. [CrossRef]
6. Sonoyama, N.; Suganuma, Y.; Kume, T.; Quan, Z. Lithium intercalation reaction into the Keggin type polyoxomolybdates. *J. Power Sources* **2011**, *196*, 6822. [CrossRef]
7. Liu, S.; Volkmer, D.; Kurth, D.G. Functional Polyoxometalate Thin Films via Electrostatic Layer-by-Layer Self-Assembly. *J. Clust. Sci.* **2003**, *14*, 405. [CrossRef]
8. So, H.; Pope, M. Origin of some charge-transfer spectra. Oxo compounds of vanadium, molybdenum, tungsten, and niobium including heteropoly anions and heteropoly blues. *Inorg. Chem.* **1972**, *11*, 1441. [CrossRef]
9. Okuhara, T.; Mizuno, N.; Misono, M. Catalytic Chemistry of Heteropoly Compounds. *Adv. Catal.* **1996**, *41*, 113.
10. Zhixia, S.; Lin, X.; Weihua, G.; Bingbing, X.; Shuping, L.; Fengyan, L. Enhanced Photoelectrochemical Performance of Nanocomposite Film Fabricated by Self-Assembly of Titanium Dioxide and Polyoxometalates. *J. Phys. Chem. C* **2010**, *114*, 5211.
11. Zhixia, S.; Fengyan, L.; Mingliang, Z.; Lin, X.; Shuna, F. A comparative study on photoelectrochemical performance of TiO_2 photoanodes enhanced by different polyoxometalates. *Electrochem. Commun.* **2013**, *30*, 38.
12. Mane, S.R.; Walekar, B.J.; Mane, R.M.; Kondalkar, V.V.; Ghanwat, V.B.; Bhosale, P.N. Molybdenum Heteropolyoxometalate Thin Films for Solar Cell Applications. *Procedia Mater. Sci.* **2014**, *6*, 1104. [CrossRef]
13. Ozer, R.R.; Ferry, J.L. Investigation of the Photocatalytic Activity of TiO_2 –Polyoxometalate Systems. *Environ. Sci. Technol.* **2001**, *35*, 3242. [CrossRef] [PubMed]
14. Pope, M.T.; Muller, A. Polyoxometalate Chemistry: An Old Field with New Dimensions in Several Disciplines. *Angew. Chem. Int. Ed. Engl.* **1991**, *30*, 34. [CrossRef]
15. Rhule, J.T.; Hill, C.L.; Judd, D.A.; Schinazi, R.F. Polyoxometalates in Medicine. *Chem. Rev.* **1998**, *98*, 327. [CrossRef]
16. Long, D.-L.; Burkholder, E.; Cronin, L. Polyoxometalate clusters, nanostructures and materials: From self assembly to designer materials and devices. *Chem. Soc. Rev.* **2007**, *36*, 105. [CrossRef]
17. Parayil, S.K.; Lee, Y.M.; Yoon, M. Photoelectrochemical solar cell properties of heteropolytungstic acid-incorporated TiO_2 nanodisc thin films. *Electrochem. Commun.* **2009**, *11*, 1211. [CrossRef]
18. Kozhevnikov, I.V. Catalysis by Heteropoly Acids and Multicomponent Polyoxometalates in Liquid-Phase Reactions. *Chem. Rev.* **1998**, *98*, 171. [CrossRef]
19. Sadakane, M.; Steckhan, E. Electrochemical Properties of Polyoxometalates as Electrocatalysts. *Chem. Rev.* **1998**, *98*, 219. [CrossRef]
20. Weinstock, I.A. Homogeneous-Phase Electron-Transfer Reactions of Polyoxometalates. *Chem. Rev.* **1998**, *98*, 113. [CrossRef]

21. Guo, Y.H.; Wang, Y.H.; Hu, C.W.; Wang, Y.H.; Wang, E.B.; Zhou, Y.C.; Feng, S.H. Microporous Polyoxometalates POMs/SiO₂: Synthesis and Photocatalytic Degradation of Aqueous Organochlorine Pesticides. *Chem. Mater.* **2000**, *12*, 3501. [[CrossRef](#)]
22. Sun, Z.; Li, F.; Xu, L.; Liu, S.; Zhao, M.; Xu, B. Effects of Dawson-Type Tungstophosphate on Photoelectrochemical Responses of Cadmium Sulfide Composite Film. *J. Phys. Chem. C* **2012**, *116*, 6420. [[CrossRef](#)]
23. Yang, Y.; Xu, L.; Li, F.; Du, X.; Sun, Z. Enhanced photovoltaic response by incorporating polyoxometalate into a phthalocyanine-sensitized electrode. *J. Mater. Chem.* **2010**, *20*, 10835. [[CrossRef](#)]
24. Soled, S.; Miseo, S.; McVicker, G.; Gates, W.E.; Gutierrez, A.; Paes, J. Preparation of bulk and supported heteropolyacid salts. *Catal. Today* **1997**, *36*, 441. [[CrossRef](#)]
25. Neeft, J.P.A.; Makkee, M.; Moulijn, J.A. Metal oxides as catalysts for the oxidation of soot. *Chem. Eng. J.* **1996**, *64*, 295. [[CrossRef](#)]
26. Hassanien, A.S.; Akl, A.A. Effect of Se addition on optical and electrical properties of chalcogenide CdSSe thin films. *Superlattices Microstruct.* **2016**, *89*, 153. [[CrossRef](#)]
27. Parry, E.P. An infrared study of pyridine adsorbed on acidic solids. Characterization of surface acidity. *J. Catal.* **1963**, *2*, 371. [[CrossRef](#)]
28. Abu-Zied, B.M.; Farrag, A.A.; Asiri, A.M. Preparation of caesium-substituted phosphomolybdic acid via solid-state ion exchange method. *Powder Technol.* **2013**, *246*, 643. [[CrossRef](#)]
29. Paul, N.; Hammond, R.B.; Hunter, T.N.; Edmondson, M.; Maxwell, L.; Biggs, S. Synthesis of nuclear waste simulants by reaction precipitation: Formation of caesium phosphomolybdate, zirconium molybdate and morphology modification with citratomolybdate complex. *Polyhedron* **2015**, *89*, 129. [[CrossRef](#)]
30. Dawei, F.; Guobao, L.; Jingcheng, H. Fabrication and electrocatalytic activities of porphyrin and 12 molybdophosphoric acid hybrid films. *J. Colloid Interface Sci.* **2010**, *351*, 151.
31. Khot, K.V.; Mali, S.S.; Ghanwat, V.B.; Kharade, S.D.; Mane, R.M.; Hong, C.K.; Bhosale, P.N. Photocurrent enhancement in a Cu₂Cd(SSe)₂ photoanode synthesized via an arrested precipitation route. *New J. Chem.* **2016**, *40*, 3277. [[CrossRef](#)]
32. Ghanwat, V.B.; Mali, S.S.; Bagade, C.S.; Khot, K.V.; Desai, N.D.; Hong, C.K.; Bhosale, P.N. Enhancement in thermoelectric performance of Cu₃SbSe₄ thin films by In(III) doping; synthesized by arrested precipitation technique. *J. Mater. Sci. Mater. Electron.* **2018**, *29*, 8793. [[CrossRef](#)]
33. Hassanien, A.S.; Akl, A.A.; El Redaf, I.M. Comparative Studies for Determining the Optical Band-gap Energy of the Novel Polycrystalline Thin ZnGa₂S₄ Films Sprayed at Different Film Thicknesses. *Res. Sq.* **2021**. [[CrossRef](#)]
34. Khalaf, M.K.; Alhilli, B.A.M.; Khudiar, A.I.; Alzahra, A.A. Influence of nanocrystalline size on optical band gap in CdSe thin films prepared by DC sputtering. *Photonics Nanostruct. Fundam. Appl.* **2016**, *18*, 59. [[CrossRef](#)]
35. Patil, S.S.; Mali, S.S.; Hong, C.K.; Bhosale, P.N. Designing of novel efficient photoactive ternary Zn_{1-x}Cu_{2x}Se thin film materials via hydrothermal route: Photoelectrochemical (PEC) cell study. *Mater. Sci. Semicond. Process.* **2020**, *105*, 104727. [[CrossRef](#)]
36. Vishwakarma, S.R.; Kumar, A.; Das, S.; Verma, A.K.; Tripathi, R.S.N. Thickness dependent properties of n-cdse thin films fabricated by electron beam evaporation technique. *Chalcogenide Lett.* **2013**, *10*, 239.
37. Xin, M.; Li, K.W.; Wang, H. Synthesis of CuS thin films by microwave assisted chemical bath deposition. *Appl. Surf. Sci.* **2009**, *256*, 1436. [[CrossRef](#)]
38. Woo, K.; Kim, Y.; Yang, W.; Kim, K.; Kim, I.; Oh, Y.; Kim, J.Y.; Moon, J. Band-gap-graded Cu₂ZnSn(S_{1-x}Se(x))₄ solar cells fabricated by an ethanol-based, particulate precursor ink route. *Sci. Rep.* **2013**, *3*, 3069. [[CrossRef](#)]
39. Tao, M.; Zhang, D.; Guan, H.; Huang, G.; Wang, X. Designation of highly efficient catalysts for one pot conversion of glycerol to lactic acid. *Sci. Rep.* **2016**, *6*, 29840. [[CrossRef](#)]
40. Haber, J.; Pamin, K.; Matachowski, L.; Napruszewska, B.; Poltowicz, J. Potassium and silver salts of tungstophosphoric acid as catalysts in dehydration of ethanol and hydration of ethylene. *J. Catal.* **2002**, *207*, 296. [[CrossRef](#)]
41. Borghese, S.; Louis, B.; Blanc, A.; Pale, P. Design of silver (I)-heteropolyacids: Toward the molecular control of reactivity in organic chemistry. *Catal. Sci. Technol.* **2011**, *1*, 981. [[CrossRef](#)]
42. Herberholz, R.; Carter, M.J. Investigation of the chalcogen interdiffusion in CuIn(TeSe)₂ thin films. *Sol. Energy Mater. Sol. Cells* **1996**, *44*, 357. [[CrossRef](#)]
43. Kite, S.V.; Sathe, D.J.; Patil, S.S.; Bhosale, P.N.; Garadkar, K.M. Nanostructured TiO₂ thin films by chemical bath deposition method for high photoelectrochemical performance. *Mater. Res. Express* **2019**, *6*, 026411. [[CrossRef](#)]
44. Ji, H.; Ju, H.; Lan, R.; Wu, P.; Sun, J.; Chao, Y.; Xun, S.; Zhu, W.; Li, H. Phosphomolybdic acid immobilized on ionic liquid-modified hexagonal boron nitride for oxidative desulfurization of fuel. *RSC Adv.* **2017**, *7*, 54266. [[CrossRef](#)]
45. Savariraj, A.D.; Viswanathan, K.K.; Prabakar, K. CuS nano flakes and nano platelets as counter electrode for quantum dots sensitized solar cells. *Electrochim. Acta* **2014**, *149*, 364. [[CrossRef](#)]
46. Sharma, K.; Sharma, V.; Sharma, S.S. Dye-Sensitized Solar Cells: Fundamentals and Current Status. *Nanoscale Res. Lett.* **2018**, *13*, 381. [[CrossRef](#)]
47. Generosi, A.; Guaragno, M.; Zhu, Q.; Proust, A.; Barrett, N.T.; Tortech, L.; Paci, B. In-Situ Energy Dispersive X-ray Reflectivity Applied to Polyoxometalate Films: An Approach to Morphology and Interface Stability Issues in Organic Photovoltaics. *Symmetry* **2020**, *12*, 1240. [[CrossRef](#)]

Disclaimer/Publisher's Note: The statements, opinions and data contained in all publications are solely those of the individual author(s) and contributor(s) and not of MDPI and/or the editor(s). MDPI and/or the editor(s) disclaim responsibility for any injury to people or property resulting from any ideas, methods, instructions or products referred to in the content.